Chapter 5:

Mixed-phase heterostructure engineering of SnS

5.1 Introduction

As one of the initial members of the orthorhombic two-dimensional (2D) material family, black phosphorene (BP) has demonstrated remarkable physicochemical properties, making it a promising candidate for nanosensor applications [1–3]. In the previous chapter, we explored how defect-engineered BP can enhance gas sensing performance due to its high defect susceptibility. In this chapter, we shift our focus to SnS, a BP-analogous material from the orthorhombic transition metal monochalcogenide (TMMC) family. SnS shares a similar structural configuration with BP but offers greater stability, as evidenced by its higher vacancy formation energy (discussed in Table 1.1) in both Sn-rich and S-rich growth environments [4]. Compared to its isostructural counterpart BP, SnS exhibits better resistance to oxidation [5].

α-SnS, also known as orthorhombic SnS, a puckered 2D TMMC material with an anisotropic structural configuration, and broken inversion symmetry in its monolayer form, has garnered significant interest due to its distinct intrinsic properties, like aeolotropic electronic and optical properties, spin-orbit splitting, and high thermoelectric coefficient [6–8]. In the recent years, SnS has become a subject of topical research due to its prospective applications in optoelectronic devices such as photovoltaics (PV) [6,9–12]. While other chalcogenide materials like CdTe, and $CuInGaSe_2$ exhibit high PV efficiencies, their use is limited by factors such as high cost and toxicity [13,14]. In contrast, SnS, with its abundance in the earth's crust and non-toxic nature, along with its suitable optical band gap for solar light absorption, offers significant advantages over other PV materials [6,10].

The effectiveness of PV devices depends on the intrinsic electronic structure of SnS. Incident light particles (photons) interact with the material, exciting electrons to the higher-energy conduction band (CB) from the lower-energy valence band (VB). This excitation leaves holes behind in the VB. The movement of these excited electrons and holes within the material generates an electric current. The pristine electronic states of SnS allow for defect-free absorption, a critical factor for developing highly efficient and effective PV devices. Therefore, preserving the intrinsic optoelectronic properties of SnS is essential for its effectiveness, to function as a photovoltaic device.

In this work, we propose stacking a monolayer of SnS with a large band gap semiconductor such as hexagonal boron nitride (*h*-BN) to preserve its intrinsic optoelectronic properties. The inert electronic and optical properties of *h*-BN monolayer is discussed in Appendix A.6. Renowned for its superior chemical and thermal stability over other 2D materials like graphene, *h*-BN has already demonstrated its effectiveness in mitigating defects in BP [15–17]. To be mentioned, that heterostructures based on similar lattice structures are extensively studied, but those with dissimilar lattices (orthorhombic-hexagonal) remain scarce, and hold promise for developing mixed-phase heterostructures in the future. The well-known electronic structure underestimation in density functional theory (DFT) is corrected by employing Green's function 'G' with screened Coulomb potential 'W' (GW) calculation established upon many-body perturbation theory (MBPT). The optical absorption (imaginary ε) spectrum of the proposed heterostructure is derived through the Bethe-Salpeter equation (BSE). We speculate that the mixed phase SnS/*h*-BN heterostructure can effectively preserve the intrinsic properties of SnS, making it a desirable prospect for next-generation PV and other optoelectronic devices.

5.2 Computational details

The calculations were done using the PWSCF code in the Quantum Espresso software suite based on DFT and plane-wave pseudopotential approach [18–21]. The generalized-gradient-approximation (GGA) with non-empirical Perdew-Burke-Ernzerhof (PBE) parameterization was used to treat the exchange-correlation functional in the calculations [22]. The electron-ion interactions were modelled using the scalar-relativistic Optimized Norm-Conserving Vanderbilt Pseudopotential (ONCVPSP) [23]. The kinetic energy cutoff (ecutwfc) and the charge density cutoff (ecutrho) for the wavefunctions was kept at 50 Ry (680 eV), and 300 Ry (4081 eV), respectively. The sampling of the primary Brillouin zone (BZ) for BNNT, monolayer SnS, SnS/BNNT heterostructures were done at 1×6×1, 6×6×1, 6×6×1 *k*-point grid, respectively, generated via the Monkhorst-Pack scheme. For a precise integration of the BZ during the non-self-consistent calculations an even denser corresponding *k*-grid of 1×18×1, 12×12×1, 12×12×1, were considered for the three structures respectively. An energy convergence threshold of 10^{-4} Ry and a force convergence threshold of 10^{-3} Ry/Bohr were used to relax the lattice and atomic parameters. The convergence criteria for self-consistent calculation were set at 10^{-8} Ry.

Semi-empirical Grimme's DFT-D2 parameter accounts for the Van der Waals (vdW) force in the heterostructure [24].

Lattice mismatch along a particular direction was calculated by,

$$\frac{\mathrm{L_{SnS}} - \mathrm{L}_{h\text{-BN}}}{\mathrm{L_{SnS}}} \times 100 \qquad \ldots(5.1)$$

here, $\mathrm{L_{SnS}}$ and $\mathrm{L}_{h\text{-BN}}$ are the lattice parameters of SnS and *h*-BN supercell along a particular direction.

The strain % on each layer along a particular direction was calculated by,

$$\frac{\mathrm{L_{hetero}} - \mathrm{L}_{\mathrm{SnS}/h\text{-BN}}}{\mathrm{L}_{\mathrm{SnS}/h\text{-BN}}} \times 100 \qquad \ldots(5.2)$$

here, $\mathrm{L_{hetero}}$ is the lattice parameter of the heterostructure along a particular direction, and $\mathrm{L}_{\mathrm{SnS}/h\text{-BN}}$ is the lattice parameter of SnS or *h*-BN supercell along the same direction.

The binding energy ($\mathrm{E_b}$) per unit cell of the heterostructure was calculated by the following formula:

$$\mathrm{E_b} = \mathrm{E}_{\mathrm{SnS}/h\text{-BN}} - \mathrm{E_{SnS}} - \mathrm{E}_{h\text{-BN}} \qquad \ldots(5.3)$$

the terms $\mathrm{E}_{\mathrm{SnS}/h\text{-BN}}$, $\mathrm{E_{SnS}}$, $\mathrm{E}_{h\text{-BN}}$ represent the total energies of the SnS/*h*-BN heterostructure, isolated SnS layer, and *h*-BN layer, respectively.

The equation to calculate the charge density difference (CDD) is as follows:

$$\triangle\rho = \rho_{\mathrm{SnS}/h\text{-BN}} - \rho_{\mathrm{SnS}} - \rho_{h\text{-BN}} \qquad \ldots(5.4)$$

where, $\rho_{\mathrm{SnS}/h\text{-BN}}$, ρ_{SnS}, $\rho_{h\text{-BN}}$ indicate the overall charge densities of the SnS/*h*-BN heterostructure, isolated SnS layer, and *h*-BN layer, respectively.

Beyond DFT, the energy levels were corrected by introducing quasiparticle interactions through GW computations based on MBPT. The quasiparticle interaction is introduced by the following non-linear equation,

$$E_{nk}^{QP} = \epsilon_{nk} + Z_{nk} < \Psi_{nk} | \Sigma\left(E_{nk}^{QP}\right) - V_{xc} | \Psi_{nk} > \qquad \ldots(5.5)$$

where the term Z_{nk} represents renormalisation factor. With the evaluation of the dynamical and static components in the self-energy (Σ), the plasmon-pole approximation

(PPA) is used to determine the single pole function frequency subjected to the dielectric matrix [25,26].

The excitonic electron-hole effect is incorporated by solving the BSE [26,27],

$$(E_{ck} - E_{vk})A^{S}_{vck} + \sum_{kv'c'} < vck|K^{eh}|v'c'k' > A^{S}_{v'c'k'} = \Omega^{s} A^{S}_{vck} \qquad \ldots(5.6)$$

where, the screened interaction between excited electrons and holes are described by the kernel term K^{eh} [26,27]. The terms A^{S}_{vck}, and Ω^{s} represent the electron-hole amplitudes, and the exciton energy, respectively. E_{ck} and E_{vk} are the quasiparticle energies of the electron and hole states. The subscripts v, c, and k represents the valence band, conduction band, and k vector, respectively. The GW+BSE computation is done using the YAMBO package [28,29].

5.3 Structural properties and stability of SnS/*h*-BN heterostructure

At first, the structural parameters of the SnS and *h*-BN monolayer were optimized using the DFT-GGA approach. The optimized unit cell parameters for SnS are found to be a = 4.05 Å and b = 4.43 Å, while for *h*-BN they are a = b = 2.52 Å. These results align well with previous reports [30,31]. Given the different geometries of the SnS and *h*-BN unit cells (orthorhombic and hexagonal, respectively), an orthorhombic unit cell of *h*-BN was adopted to build the heterostructure. The optimized lattice parameters for the orthorhombic unit cell of *h*-BN are a = 2.52 Å, b = 4.36 Å. The SnS/*h*-BN heterostructure was modelled using a 2×1 supercell of SnS and a 3×1 orthorhombic supercell of *h*-BN (Fig. 5.1). The following transformation matrix was used to model the orthorhombic unit cell of *h*-BN.

$$T_M = \begin{pmatrix} 1 & -1 & 0 \\ 1 & 1 & 0 \\ 0 & 0 & 1 \end{pmatrix}$$

A schematic illustration of modelling the mixed-phase heterostructure is provided in Fig. 5.2. The ground state energy of the SnS/*h*-BN heterostructure was found to be minimal when the cell parameters are a = 8.00 Å, b = 4.40 Å (Fig. 5.1). The lattice mismatch in the SnS/*h*-BN heterostructure is 6.67% and 1.58%. The values are listed in Table 5.1. While a 6.67% mismatch might seem marginally high, it is experimentally feasible because the growth of vdW heterostructures depends on vdW interactions rather than chemical bonding at the interface [32]. Heterostructures with highly mismatched lattice parameters, such as

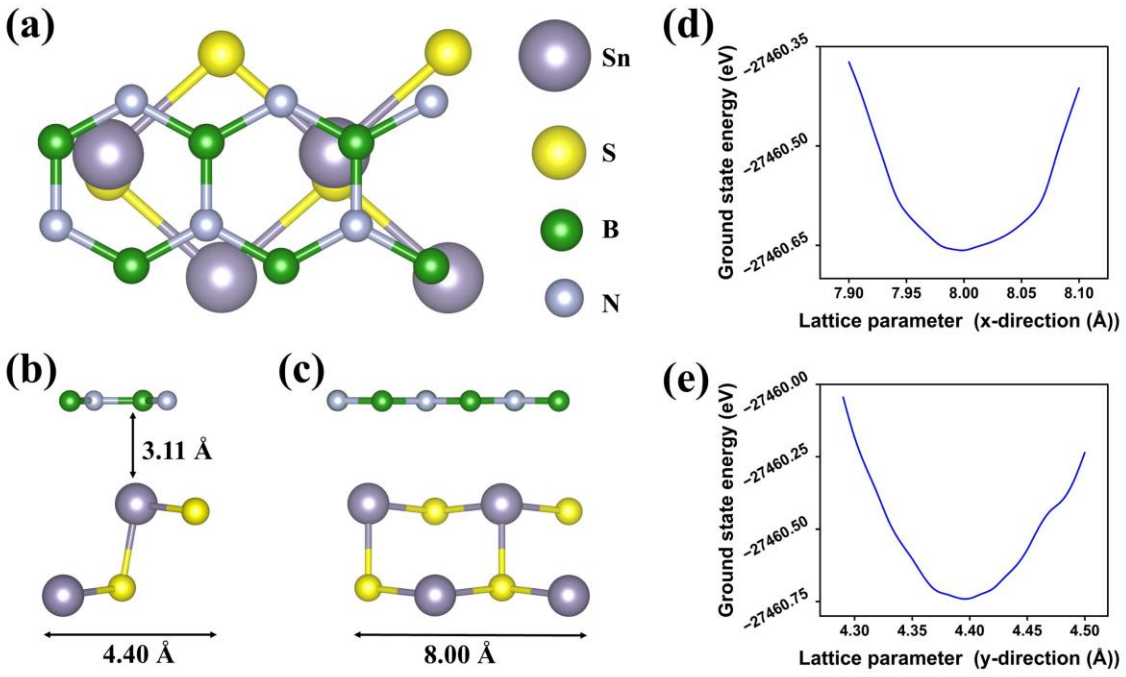

Figure 5.1: *(a) Top view, (b,c) side view of mixed phase SnS/h-BN heterostructure; (d,e) convergence test of lattice parameters vs. ground state energy.*

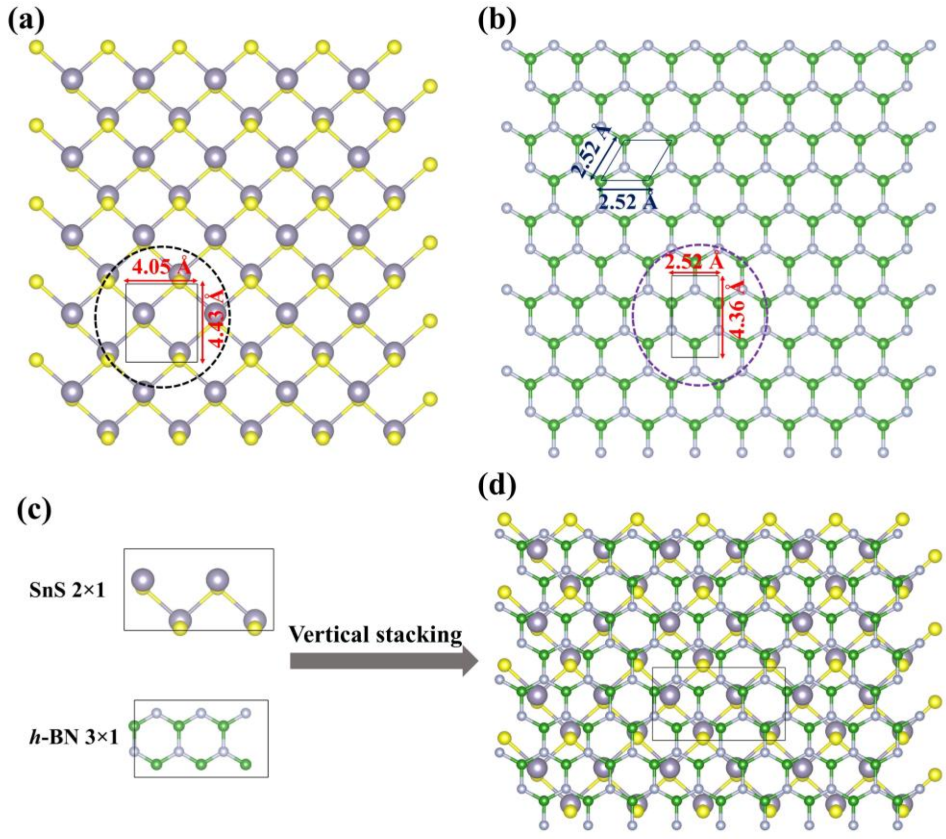

Figure 5.2: *Schematic representing the modelling process of the SnS/h-BN heterostructure.*

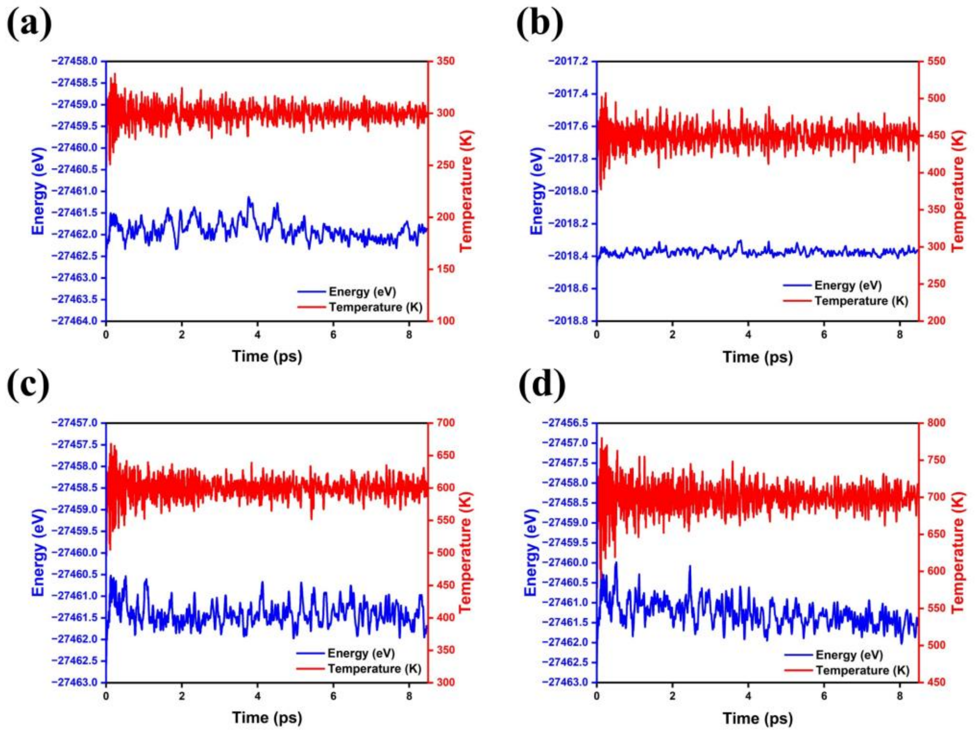

Figure 5.3: *AIMD simulation at (a) 300 K, (b) 450 K, (c) 600 K, and (d) 700 K (the axis on the left side of the figures represents the energy of the heterostructure and the axis on the right side of the figures represents the temperature scale).*

Table 5.1: Lattice parameters of the monolayer supercells and the strain experienced by them within the heterostructure.

		SnS		*h*-BN		Heterostructure
Cell size		**1×1**	**2×1**	**1×1**	**3×1**	**1×1**
Lattice parameters	**a**	4.05 Å	8.1 Å	2.52 Å	7.56 Å	8.00 Å
	b	4.43 Å	4.43 Å	4.36 Å	4.36 Å	4.40 Å
Strain %	**a**		-1.23%		5.82%	
	b		-0.67%		0.92%	

$SnSe_2/MoS_2$ (20%) and In_2Se_3/MoS_2 (20%), have already been synthesized experimentally [33,34]. Additionally, a recent computational study on electric field-controlled type-I to type-II band conversion in BP/SnS heterostructure also reported a lattice mismatch of 7% [35]. As shown in Fig. 5.1(b) the optimized interlayer separation between SnS and *h*-BN is 3.11 Å.

The heterostructure possesses a stable interface binding energy of -1.91 eV per unit cell. The negative value of binding energy (E_b) suggests that the heterostructure is structurally stable and energetically favourable. To further evaluate the stability of the SnS/h-BN heterostructure, *ab initio* molecular dynamics (AIMD) calculations were executed at room temperature (300 K), 450 K, 600 K and 700 K. The maximum energy fluctuations in the total energy of the heterostructure over 8.5 ps at these temperatures were compared to the binding energy (E_b = -1.91 eV) of the heterostructure. At room temperature and 450 K, the maximum energy fluctuations are 0.27 eV and 0.16 eV, respectively. This suggests that the ideal temperature for experimentally synthesizing the mixed-phase SnS/h-BN heterostructure is around 450 K. At 600 K, the energy fluctuation increases to 1.87 eV, nearly equal to the binding energy of the heterostructure. At 700 K, the energy fluctuation (~2.61 eV) due to thermal agitation surpasses the binding energy, potentially causing the heterostructure layers to separate. The minimal energy fluctuations observed over a period of 8.5 ps suggest that up to 600 K the heterostructure is thermally stable (Fig. 5.3).

5.4 Interlayer charge transport and built-in electric fields

From the charge density difference plot (Fig. 5.4(a)), it is evident that charges accumulate near the surface of h-BN. This occurs because nitrogen has the highest electronegativity among the four atomic species in the heterostructure. Bader charge analysis reveals that 0.032 e has been transferred from the surface of SnS to the surface of h-BN. Consequently, there is a built-in electric field between the two surfaces, directing from h-BN to SnS. This built-in electric field at the junction of the heterostructure can be easily visualized from Fig. 5.4(b). The difference in electrostatic potential (ΔV_{hetero}) between the two surfaces is 0.61 eV. This potential difference drives the charge flow between the surfaces. Apart from the potential difference at the surface interface, there is a potential difference between the two atomic layers of SnS (ΔV_{SnS} = 0.14 eV). The charge dynamics at the heterostructure interface cause non-uniformity in the electrostatic potential between the two atomic layers within SnS (Fig. 5.4(a)). Such intralayer potential difference is not generally observed in freestanding SnS monolayer (shown in the inset of Fig. 5.4(b)) or other vertical SnS based heterostructure reported in literature [36]. The built-in interlayer ($\vec{E}_{hetero}$) and intralayer ($\vec{E}_{SnS}$) electric fields in the heterostructure play a crucial role in spatially separating electron-hole pairs, thereby significantly enhancing the ability to improve the translation of photogenerated charges and improving the PV efficiency (discussed later in section 5.6).

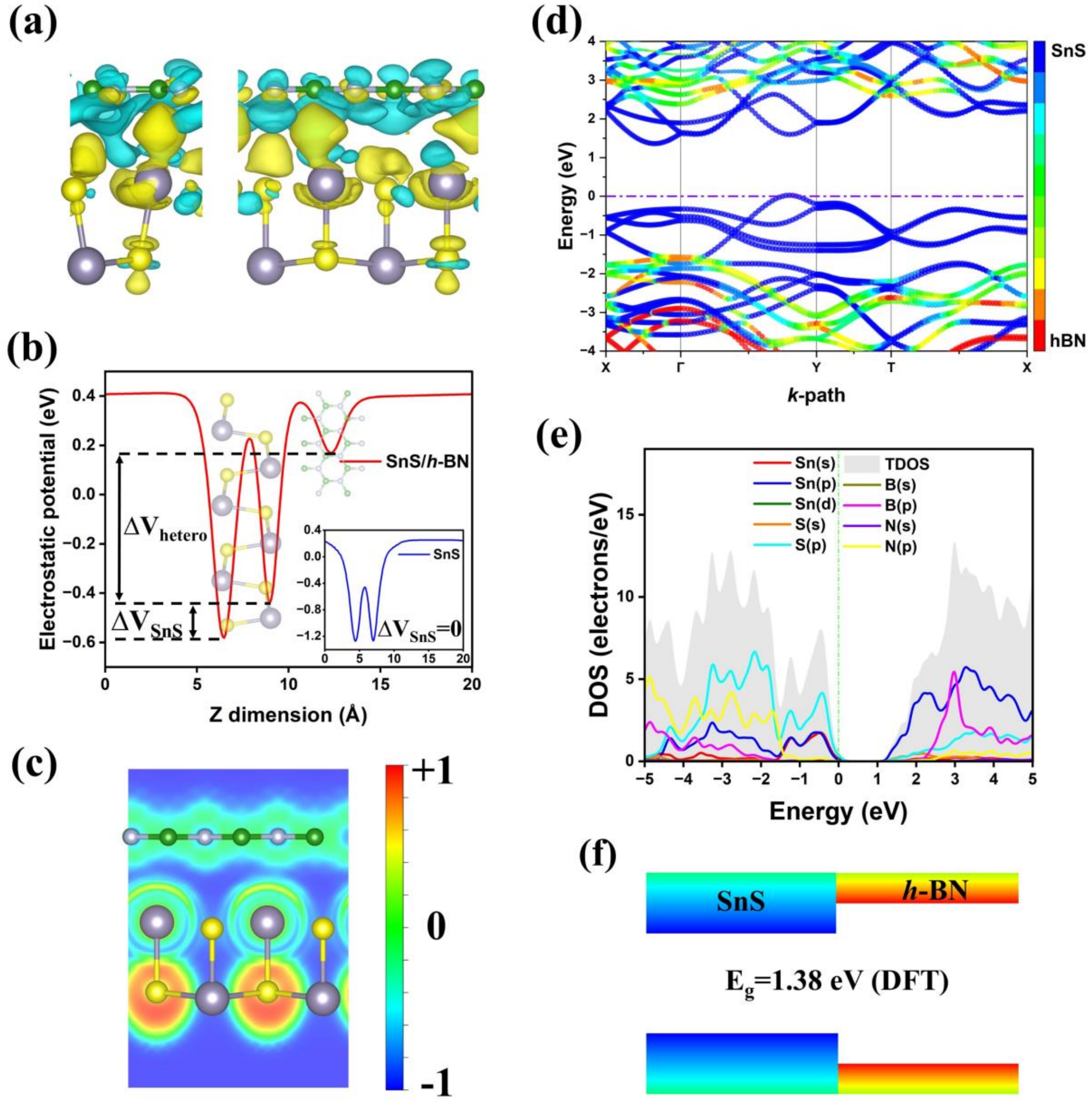

Figure 5.4: *(a) Charge density difference plot of SnS/h-BN heterostructure (cyan and yellow colour represents the accumulation and depletion of charges, respectively); (b) electrostatic potential along the z-direction of SnS/h-BN heterostructure (inset: electrostatic potential of SnS monolayer); (c) electron localization function (elf) plot of SnS/h-BN heterostructure (the blue to red colour bar indicates the lowest (-1) to highest (1) value; (d) layer projected electronic band structure plotted along the X-Γ-Y-T-X high symmetric path (blue and red colour indicates the contribution from the SnS and h-BN monolayers, respectively); (e) orbital projected density of states (PDOS) of SnS/h-BN heterostructure; and (f) schematic showing the straddling type-I band alignment of SnS/h-BN heterostructure.*

The electron localization function in Fig. 5.4(c) evidently illustrates that the bonding between the SnS and *h*-BN layers is vdW in nature.

5.5 Preserved electronic properties of SnS

The electronic properties of the heterostructure, calculated using DFT-GGA, reveal a type-I band alignment (Fig. 5.4(d,e)). Both the conduction band minimum (CBM) and valence band maximum (VBM) predominantly originate from the SnS layer (Fig. 5.4(d)). Near the Fermi level, most bands are primarily composed of SnS, while the *h*-BN bands lie deeper and farther away. The projected density of states (PDOS) indicates that Sn 5*p* orbitals contribute to the conduction bands near the Fermi level, while S *3p* orbitals dominate the valence bands (Fig. 5.4(e)). This suggests that the intrinsic electronic properties of SnS, particularly the states in the vicinity of the Fermi level, are well preserved by the deep-lying orbitals of *h*-BN. The schematic represented in Fig. 5.4(f) depicts the straddling type-I band structure of the heterostructure. This straddling band alignment results in an indirect band gap, with the VBM positioned along the Γ-Y direction and the CBM along the Γ-X direction. At the DFT-GGA level, the indirect band gap of the heterostructure is 1.38 eV.

To assess the extent to which SnS electronic states are preserved in the heterostructure, we compare the straddling band structure of SnS/*h*-BN to the band structure of a freestanding

Table 5.2: Indirect and direct band gaps of SnS/*h*-BN heterostructure and SnS monolayer along with their direction in the BZ calculated at the GW and DFT-GGA level. The last column shows the difference between the band gaps of SnS monolayer and SnS/*h*-BN heterostructure.

Nature of gap	**Calculation level**	**SnS**	**SnS/*h*-BN**	**ΔE_g**
		Gap (direction)	**Gap (direction)**	
Indirect	GW	2.28 eV (Γ-Y to Γ-X)	2.20 eV (Γ-Y to Γ-X)	0.08 eV
	DFT-GGA	1.52 eV (Γ-Y to Γ-X)	1.38 eV (Γ-Y to Γ-X)	0.14 eV
Direct	GW	2.50 eV (Γ-Y)	2.47 eV (Γ-Y)	0.03 eV
		2.83 eV (Γ-X)	2.72 eV (Γ-X)	0.11 eV
	DFT-GGA	1.72 eV (Γ-Y)	1.60 eV (Γ-Y)	0.12 eV
		1.94 eV (Γ-X)	1.70 eV (Γ-X)	0.24 eV

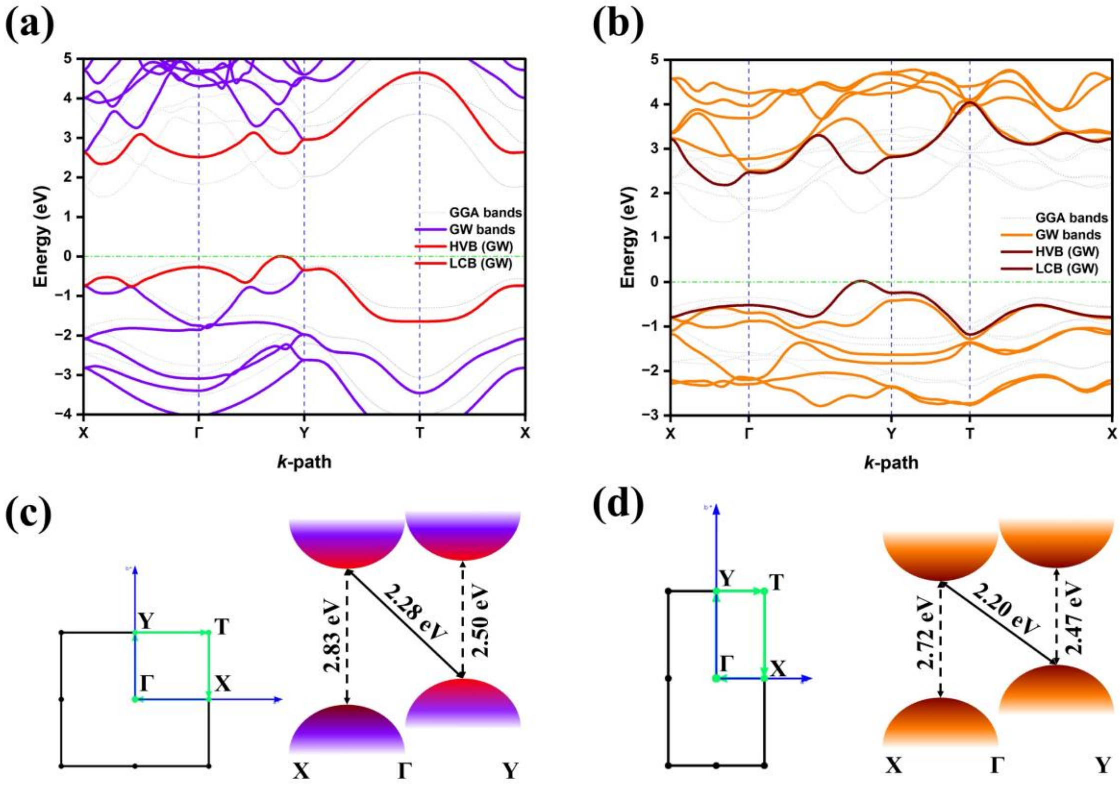

Figure 5.5: *GW band structure of (a) SnS monolayer, (b) SnS/h-BN heterostructure (the dotted lines in the figures indicates to the bands calculated using DFT-GGA approach; the quasiparticle GW bands in (a) and (b) are represented by the violet, and the orange lines, respectively; the highest valence band (HVB) and the lowest conduction band (LCB) in (a), and (b) are represented by the red and wine coloured line, respectively); (c, d) illustrates the BZ and schematic representation of band gaps of SnS, and SnS/h-BN, respectively.*

SnS monolayer. At DFT-GGA level, the SnS monolayer has an indirect band gap of 1.52 eV (represented by the dotted lines in Fig. 5.5(a)). The VBM in SnS monolayer is along Γ-Y direction and the CBM is along Γ-X direction. The results for SnS monolayer align well with previous reports [6,10,30]. As discussed earlier, the heterostructure shares this indirect band gap characteristics with the monolayer SnS. The direct bandgaps of both SnS monolayer and the SnS/*h*-BN heterostructure exhibit their minimum direct bandgaps along the Γ-Y direction with DFT-GGA values of 1.72 eV and 1.60 eV, respectively (Table 5.2). Along the Γ-X direction, the corresponding values are 1.94 eV and 1.70 eV. While the overall bandgap trends are similar between the monolayer and heterostructure, notable differences emerge in the band gap values. The indirect band gap in the heterostructure is dropped by 0.14 eV, whereas the direct band gap along Γ-Y and Γ-X valleys are red shifted by 0.12 eV and 0.24 eV, respectively. We surmise that these significant discrepancies in the band gap values between SnS monolayer and the SnS/*h*-BN heterostructure lies in the inefficiency of DFT-GGA calculation level.

DFT often underestimates the electronic band gap of a material as it excludes electron-electron and electron-ion interactions. For an accurate calculation of a material's electronic structure and to compare the results with experimental studies, it is crucial to incorporate these missing interactions. In addition, including these many-body interactions can yield precise and accurate electronic structures. For instance, while DFT-GGA predicts a direct bandgap for *h*-BN monolayer, quasiparticle calculations reveal an indirect bandgap along the K-Γ direction [15,37]. To obtain a precise electronic band structure of the SnS/*h*-BN heterostructure, we incorporate quasiparticle-corrected GW calculations. Our quasiparticle-incorporated band structures for SnS (Fig. 5.5(a)) and the SnS/*h*-BN heterostructure (Fig. 5.5(b)) show significant corrections compared to the DFT-GGA band structures (Table 5.2). While the shape of the band structure remains invariant and closely follows the band alignment of DFT-GGA calculation, the band gap is significantly corrected. The GW calculations for SnS monolayer are in agreement with the existing literatures [38–40]. The quasiparticle corrected minimum band gap of the heterostructure is 2.20 eV. The minimum direct band gap along the Γ-Y and Γ-X valley are 2.47 eV and 2.72 eV, respectively. As shown in Table 5.2 and illustrated in the schematic Fig. 5.5(c,d), compared to DFT-GGA band gaps, the indirect band gap of the monolayer and the heterostructure now differ by marginal 0.08 eV, and the direct band gap along Γ-Y and Γ-X valley differ by significantly lower values of 0.03 eV and 0.11 eV, respectively. Thus, the quasiparticle corrected band structure of the SnS/*h*-BN heterostructure suggests that the band gaps of the SnS/*h*-BN heterostructure coincides closely with the band gaps of SnS monolayer. These band gaps, specifically the minimum direct gaps, play the most significant role in the absorption phenomena of SnS based optoelectronic devices.

Although the band gaps of SnS and SnS/*h*-BN heterostructure are closely aligned, there are some noticeable changes in the shape of the band structure along the Γ-X and T-X valleys. A closure inspection reveals that the dispersion of the band energy in these valleys differs between SnS monolayer and SnS/*h*-BN heterostructure. These modifications in the band dispersion may be attributed to two factors: (i) the compressive strain imposed on SnS in the heterostructure, or (ii) the interlayer coupling of SnS with *h*-BN. In the SnS/*h*-BN heterostructure, the SnS monolayer experiences compressive strain of 1.23% along the *x*-direction and 0.67% along the *y*-direction (Table 5.1). Although strain can alter the band gap in SnS, it is unlikely to be the key factor in shaping the E-*k* diagram [41,42]. To confirm this, we examined the electronic band structure of the SnS/*h*-BN heterostructure without imposing strain on the SnS surface (Fig. A.7). This calculation was done at the DFT-GGA level, as the quasiparticle band structure imitates the shape of the DFT-GGA band structure of the heterostructure. We found that even with 0% strain, the band dispersion along Γ-X and T-X in the heterostructure remains different from that in the SnS monolayer. This confirms that the observed changes in band curvature originate from interlayer coupling between SnS and *h*-BN within the heterostructure. Although the *h*-BN orbitals lie deep in the CB and VB regions, the interplay between the orbital states of the two surfaces is significant enough to modify the band curvature of straddling SnS.

These modifications in the band dispersion can substantially impact charge carrier mobility within the heterostructure, subsequently affecting its optical absorption properties. To assess this, we calculated the effective mass of charge carriers in the highest valence band (HVB) and lowest conduction band (LCB) for both the SnS/*h*-BN heterostructure and the SnS monolayer at the extremum band positions (Table 5.3). While most effective masses remain comparable between the two systems, the hole mass along the Γ-X valley is somewhat larger in the heterostructure due to a less dispersive band curve. This slightly reduces the hole mobility in the Γ-X direction. However, this less dispersive band curve preserved by *h*-BN is anticipated to have higher carrier mobility compared defective SnS, which has even flatter defect states [5]. Furthermore, the built-in intralayer electric field ($\vec{E}_{SnS}$) is expected to compensate for reduced mobility and enhance the transport of photogenerated carriers within their respective bands.

Table 5.3: Calculated charge carrier effective mass of SnS/*h*-BN heterostructure and SnS monolayer.

Band valley		**SnS**	**SnS/*h*-BN**
	Carrier	**$m^*(m_0)$**	**$m^*(m_0)$**
Γ-X	electron	0.08	0.04
	hole	0.24	0.38
Γ-Y	electron	0.06	0.06
	hole	0.07	0.08

5.6 Intralayer excitons in presence of electric field

Due to the weak dielectric screening in 2D materials, excitonic effects play a vital role in their optical properties and the performance of optoelectronic devices [39]. By solving BSE, we can obtain the direct band-to-band transitions, which can be compared with the experimental observations of absorption [38]. The imaginary part of the macroscopic dielectric function (Im ε) is presented in Fig. 5.6(a) for linearly polarized incident light along x- and y-directions. To better understand the excitonic effects, we calculated the optical absorption spectra both with electron-hole (w/eh) and without electron-hole (wo/eh) interactions. The energy difference between the GW direct electronic band gap and the excitonic peak in the spectra is considered as the BSE exciton binding energy (EBE). As anticipated from the electronic structure, the first excitonic peak (A_{SnS}) in SnS/*h*-BN heterostructure and the SnS monolayer arises at 2.21 eV and 2.17 eV, respectively, due to incident polarization along the y-direction (Fig. 5.6(a,b)). The second excitonic peak (B_{SnS}) in the heterostructure and the monolayer appears at 2.47 eV, and 2.52 eV, respectively (Table 5.4). This second peak is due to light incident along the x-direction. The small difference in the optical band gaps is due to the reduced direct band gaps in the heterostructure, caused by the interlayer vdW coupling of SnS and *h*-BN, as discussed earlier in the electronic properties section. The vertical drop lines in Fig. 5.6(a) depict the

Table 5.4: The excitonic peak positions and exciton binding energy (EBE) of SnS/*h*-BN heterostructure (Fig. 5.6(a)) and SnS monolayer (Fig. 5.6(b)) along with their respective direct band gap position in the BZ momentum space. The last two rows show the results of SnS monolayer under the compressive strain of 1.23% and 0.67% along the x- and y-direction, respectively.

System	*k*-valley	Direct band gap	Exciton peak	EBE
SnS/*h*-BN	Γ-Y	2.47 eV	2.21 eV	0.26 eV
	Γ-X	2.72 eV	2.47 eV	0.25 eV
SnS monolayer	Γ-Y	2.50 eV	2.17 eV	0.33 eV
	Γ-X	2.83 eV	2.52 eV	0.31 eV
SnS monolayer (strained)	Γ-Y	2.48 eV	2.16 eV	0.32 eV
	Γ-X	2.72 eV	2.41 eV	0.31 eV

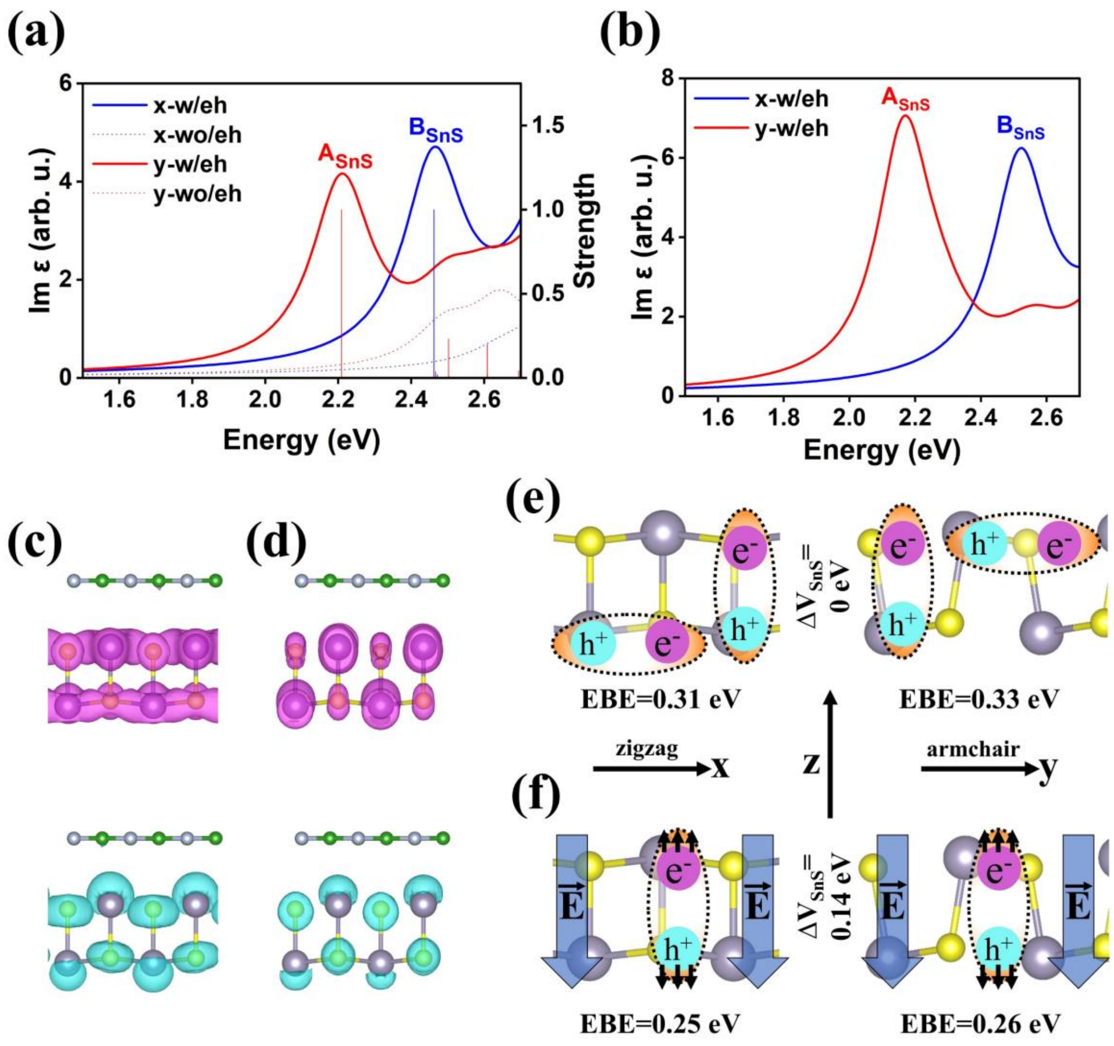

Figure 5.6: *Optical absorption spectra of (a) SnS/h-BN heterostructure (the excitonic strength is indicated by the vertical drop line in a normalized scale of 0 to 1), and (b) SnS monolayer; average electron-hole density of (c)* A_{SnS}*, and (d)* B_{SnS} *exciton in the heterostructure (the magenta (top panel) and the cyan (bottom panel) colour represents the electron and hole density, respectively); schematic demonstrating the electron-hole pairs in (e) monolayer SnS without intralayer electric field, and (f) SnS/h-BN heterostructure with intralayer electric field (the solid black arrows on electrons and hole indicates the direction of force due to the electric field).*

excitonic strengths in a normalized scale of 0 to 1 (refer to the axis on the right). Both the excitons at 2.21 eV and 2.47 eV along two directions have the strength ~1, indicating they are the brightest excitons in the heterostructure. The other excitons having strength ~0 are the dark excitons. From the electron-hole average density plots, it is evident that the bright excitons along the two-polarization direction are intralayer and confined to SnS surface (Fig. 5.6(c,d)).

Comparing the EBEs of the monolayer and heterostructure indicates that A_{SnS} and B_{SnS} in the heterostructure are weakly bound (Table 5.4). This may be caused by the small compressive strain experienced by the SnS surface within the heterostructure or the intrinsic electric field arising from the non-uniform charge dynamics in the heterostructure. It is well known that the electronic and optical properties of 2D materials and their heterostructures are highly sensitive to strain effects. As discussed earlier, the SnS surface experiences a small compressive strain along its two polarisation axes, which may influence the binding energies of A_{SnS} and B_{SnS}. To explore the effect of strain on A_{SnS} and B_{SnS}, we solved the BSE for SnS monolayer under compressive strain of 1.23% and 0.67% along its two coordinate axes, x and y, respectively (Table 5.4). The results clearly indicate that the compressive strain reduces the electronic band gap of SnS. However, despite this reduction, the exciton binding energy remains unaffected, as the optical band gap decreases proportionally. Thus, the compressive strain is not the cause of the weaker exciton binding in the heterostructure. Intrinsic electric field also plays a crucial role in spatially separating electron-hole pairs, specifically in heterojunctions with interlayer excitons [43–46]. As the electrons and holes are spatially separated across different vertical surfaces, the interlayer electric field assists in further weakening the EBEs in such heterostructures. However, in SnS/*h*-BN heterostructure, A_{SnS} and B_{SnS} are confined to SnS surface, meaning they are not affected by the interlayer electric field $\vec{E}_{hetero}$, but can be significantly influenced by the intralayer electric field $\vec{E}_{SnS}$. It is to be mentioned that the $\vec{E}_{SnS}$ is directed along the *z*-axis and will affect the electron-hole pairs that have spatial separation along the *z*-direction. Given the two atomic layered structure, it is possible for the electrons and holes in SnS to have spatial separation along the *z*-direction. This can also be visualised from the average electron-hole density plot of A_{SnS} and B_{SnS} shown in Fig. 5.6(c,d). The schematic in Fig. 5.6(e) illustrates the spatially separated electron-hole pairs in monolayer SnS along the zigzag and armchair direction. In SnS/*h*-BN heterostructure, the electron-hole pairs with spatial z-component separation are influenced by the vertical $\vec{E}_{SnS}$ (Fig. 5.6(f)). The electron in such a case will drift in the direction opposite to the electric field, while the hole will move along the direction of the field. Therefore, the weak EBEs of A_{SnS} and B_{SnS}, in the heterostructure, is attributed to the vertical intralayer electric field, $\vec{E}_{SnS}$, which promotes exciton dissociation, and enhances recombination lifetime and charge transport.

This characteristic can significantly benefit SnS-based photovoltaic and other optoelectronic devices.

5.7 Conclusion

This study investigates the electronic and excitonic properties of SnS monolayer stacked with *h*-BN for the potential application in optoelectronic devices. Structural optimizations using DFT-GGA and stability analyses via AIMD confirm structural and thermal stability (up to 600 K) of the SnS/*h*-BN heterostructure. Two built-in electric fields, namely interlayer $\vec{\mathrm{E}}_{\mathrm{hetero}}$, and intralayer $\vec{\mathrm{E}}_{\mathrm{SnS}}$ arises due to the charge transfer between SnS and *h*-BN surfaces. Electronic property analysis reveals a type-I straddling band alignment with an indirect band gap of 1.38 eV, corrected to 2.20 eV using quasiparticle GW calculations. Both the CBM and VBM originate primarily from the SnS layer, preserving its intrinsic electronic properties. Excitonic effects, analysed through optical absorption spectra, show that the first excitonic peak occurs at 2.21 eV for the heterostructure and 2.17 eV for the monolayer, with a second peak at 2.47 eV and 2.52 eV, respectively. These similar excitonic characteristics underscore the well-preserved optimal optical absorption of SnS in the heterostructure. Effective mass calculations indicate comparable charge carrier masses between the heterostructure and the monolayer, with a slight increase in hole mass along the Γ-X valley in the heterostructure. This reduction in hole mobility is offset by the intralayer electric field. The intralayer electric field, $\vec{\mathrm{E}}_{\mathrm{SnS}}$, produced by the non-uniform charge dynamics of the heterostructure, reduces the EBE of $\mathrm{A}_{\mathrm{SnS}}$ and $\mathrm{B}_{\mathrm{SnS}}$ from 0.33 eV to 0.26 eV and 0.31 eV to 0.25 eV, respectively, increasing the recombination lifetime of the excitons.

In conclusion, SnS/*h*-BN heterostructure combines electronic properties of SnS with the stability of *h*-BN. Weakly bound excitons, effective charge separation, and photogenerated charge transport enhancements via built-in intralayer electric field can significantly enhance the performance of SnS-based photovoltaic and optoelectronic devices, making SnS/*h*-BN heterostructure promising candidates for future optoelectronic applications.

References

[1] Talukdar, D., Mohanta, D., Ahmed, G. A. Nitrogen Doped Compound Defect in Black Phosphorene for Enhanced Gas sensing. *Surfaces and Interfaces*, 51: 104699, 2024.

[2] Kaewmaraya, T., Ngamwongwan, L., Moontragoon, P., Karton, A., Hussain, T. Drastic improvement in gas-sensing characteristics of phosphorene nanosheets under vacancy defects and elemental functionalization. *The Journal of Physical Chemistry C*, 122(35): 20186–20193, 2018.

[3] Suvansinpan, N., Hussain, F., Zhang, G., Chiu, C. H., Cai, Y., Zhang, Y. W. Substitutionally doped phosphorene: Electronic properties and gas sensing. *Nanotechnology*, 27(6): 065708, 2016.

[4] Ullah, H., Kim, H. J., Shin, Y. H. Influences of vacancy and doping on electronic and magnetic properties of monolayer SnS. *Journal of Applied Physics*, 124(6), 2018.

[5] Gomes, L. C., Carvalho, A., Castro Neto, A. H. Vacancies and oxidation of two-dimensional group-IV monochalcogenides. *Physical Review B*, 94(5): 054103, 2016.

[6] Gomes, L. C., Carvalho, A. Phosphorene analogues: Isoelectronic two-dimensional group-IV monochalcogenides with orthorhombic structure. *Physical Review B - Condensed Matter and Materials Physics*, 92(8): 085406, 2015.

[7] He, W., Ang, R., Zhao, L. D. Remarkable electron and phonon transports in low-cost SnS: a new promising thermoelectric material. *Science China Materials*, 65(5): 1143–1155, 2022.

[8] Li, Z., Su, X., Tang, X. Doping Achieves High Thermoelectric Performance in SnS: A First-Principles Study. *ACS Applied Materials & Interfaces*, 14(5): 6916–6925, 2022.

[9] Green, M., Dunlop, E., Hohl-Ebinger, J., Yoshita, M., Kopidakis, N., Hao, X. Solar cell efficiency tables (version 57). *Progress in photovoltaics: research and applications*, 29(1): 3–15, 2021.

[10] Tritsaris, G. A., Malone, B. D., Kaxiras, E. Optoelectronic properties of single-layer, double-layer, and bulk tin sulfide: A theoretical study. *Journal of Applied Physics*, 113(23), 2013.

[11] Repins, I., Contreras, M.A., Egaas, B., DeHart, C., Scharf, J., Perkins, C.L., To, B. and Noufi, R. 19.9%-efficient ZnO/CdS/$CuInGaSe_2$ solar cell with 81.2% fill factor. *Progress in Photovoltaics: Research and applications*, *16*(3): 235–239, 2008.

[12] Nanae, R., Kitamura, S., Chang, Y.R., Kanahashi, K., Nishimura, T., Moqbel, R., Lin, K.H., Maruyama, M., Gao, Y., Okada, S. and Qi, K. Bulk Photovoltaic Effect in Single Ferroelectric Domain of SnS Crystal and Control of Local Polarization by Strain. *Advanced Functional Materials*, 34(41): 2406140, 2024.

[13] Genchi, G., Sinicropi, M. S., Lauria, G., Carocci, A., Catalano, A. The effects of cadmium toxicity. *International journal of environmental research and public health*, 17(11): 3782, 2020.

[14] Sverdrup, H. U., Ragnarsdottir, K. V., Koca, D. On modelling the global copper mining rates, market supply, copper price and the end of copper reserves. *Resources, Conservation and Recycling*, 87: 158–174, 2014.

[15] Talukdar, D., Bora, S. S., Ahmed, G. A. Electronic, optical, and adsorption properties of Li-doped hexagonal boron nitride: a GW approach. *Physical Chemistry Chemical Physics*, 26(5): 4021–4028, 2024.

[16] Wang, J., Zhang, L., Wang, L., Lei, W., Wu, Z. Two-dimensional boron nitride for electronics and energy applications. *Energy & Environmental Materials*, *5*(1): 10–44, 2022.

[17] Constantinescu, G. C., Hine, N. D. M. Multipurpose black-phosphorus/hBN heterostructures. *Nano letters*, 16(4): 2586–2594, 2016.

[18] Giannozzi, P., Baroni, S., Bonini, N., Calandra, M., Car, R., Cavazzoni, C., Ceresoli, D., Chiarotti, G.L., Cococcioni, M., Dabo, I., Dal Corso, A. QUANTUM ESPRESSO: a modular and open-source software project for quantum simulations of materials. *Journal of physics: Condensed matter*, 21(39): 395502, 2009.

[19] Giannozzi, P., Andreussi, O., Brumme, T., Bunau, O., Nardelli, M.B., Calandra, M., Car, R., Cavazzoni, C., Ceresoli, D., Cococcioni, M., Colonna, N. Advanced capabilities for materials modelling with Quantum ESPRESSO. *Journal of physics: Condensed matter*, 29(46): 465901, 2017.

[20] Carnimeo, I., Affinito, F., Baroni, S., Baseggio, O., Bellentani, L., Bertossa, R., Delugas, P.D., Ruffino, F.F., Orlandini, S., Spiga, F., Giannozzi, P. Quantum ESPRESSO: One Further Step toward the Exascale. *Journal of Chemical Theory and Computation*,19(2): 6992–7006, 2023.

[21] Giannozzi, P., Baseggio, O., Bonfà, P., Brunato, D., Car, R., Carnimeo, I., Cavazzoni, C., De Gironcoli, S., Delugas, P., Ferrari Ruffino, F., Ferretti, A. Quantum ESPRESSO toward the exascale. *The Journal of chemical physics*, 152(15), 2020.

[22] Perdew, J. P., Burke, K., Ernzerhof, M. Generalized gradient approximation made simple. *Physical review letters*, 77(18): 3865, 1996.

[23] Hamann, D. R. Optimized norm-conserving Vanderbilt pseudopotentials. *Physical Review B—Condensed Matter and Materials Physics*, 88(8): 085117, 2013.

[24] Barone, V., Casarin, M., Forrer, D., Pavone, M., Sambi, M., Vittadini, A. Role and effective treatment of dispersive forces in materials: Polyethylene and graphite crystals as test cases. *Journal of Computational Chemistry*, 30(6): 934–939, 2009.

[25] Onida, G., Reining, L., Rubio, A. Electronic excitations: density-functional versus many-body Green's-function approaches. *Reviews of modern physics*, 74(2): 601, 2002.

[26] Rohlfing, M., Louie, S. G. Electron-hole excitations and optical spectra from first principles. *Physical Review B*, 62(8): 4927, 2000.

[27] Strinati, G. Effects of dynamical screening on resonances at inner-shell thresholds in semiconductors. *Physical Review B*, 29(10): 5718, 1984.

[28] Sangalli, D., Ferretti, A., Miranda, H., Attaccalite, C., Marri, I., Cannuccia, E., Melo, P., Marsili, M., Paleari, F., Marrazzo, A., Prandini, G. Many-body

perturbation theory calculations using the yambo code. *Journal of Physics: Condensed Matter*, 31(32): 325902, 2019.

[29] Marini, A., Hogan, C., Grüning, M., Varsano, D. Yambo: an ab initio tool for excited state calculations. *Computer Physics Communications*, 180(8): 1392–1403, 2009.

[30] C Gomes, L., Carvalho, A. Electronic and optical properties of low-dimensional group-IV monochalcogenides. *Journal of Applied Physics*, 128(12), 2020.

[31] Galvani, T., Paleari, F., Miranda, H.P., Molina-Sánchez, A., Wirtz, L., Latil, S., Amara, H., Ducastelle, F. Excitons in boron nitride single layer. *Physical Review B*, 94(12): 125303, 2016.

[32] Koma, A. Van der Waals epitaxy for highly lattice-mismatched systems. *Journal of Crystal Growth*, 201: 236–241, 1999.

[33] Zhou, X., Zhou, N., Li, C., Song, H., Zhang, Q., Hu, X., Gan, L., Li, H., Lü, J., Luo, J., Xiong, J. Vertical heterostructures based on $SnSe_2/MoS_2$ for high performance photodetectors. *2D Materials*, *4*(2): 025048, 2017.

[34] Zou, Z., Li, D., Liang, J., Zhang, X., Liu, H., Zhu, C., Yang, X., Li, L., Zheng, B., Sun, X., Zeng, Z. Epitaxial synthesis of ultrathin β-In_2Se_3/MoS_2 heterostructures with high visible/near-infrared photoresponse. *Nanoscale*, 12(11): 6480–6488, 2020.

[35] Chen, J. L., Wang, X. X., Shi, L. J. Electric field controlled type-I and type-II conversion of BP/SnS van der Waals heterostructure. *Journal of Physics: Condensed Matter*, 33(26): 265301, 2021.

[36] Hassan, A., Nazir, M. A., Shen, Y., Guo, Y., Kang, W., Wang, Q. First-principles study of the structural, electronic, and enhanced optical properties of SnS/TaS_2 heterojunction. *ACS Applied Materials & Interfaces*, 14(1): 2177–2184, 2021.

[37] Kirchhoff, A., Deilmann, T., Krüger, P., Rohlfing, M. Electronic and optical properties of a hexagonal boron nitride monolayer in its pristine form and with point defects from first principles. *Physical Review B*, 106(4): 045118, 2022.

[38] Tuttle, B. R., Alhassan, S. M., Pantelides, S. T. Large excitonic effects in group-IV sulfide monolayers. *Physical Review B*, 92(23): 235405, 2015.

[39] Xu, L., Yang, M., Wang, S. J., Feng, Y. P. Electronic and optical properties of the monolayer group-IV monochalcogenides MX (M= Ge, Sn; X= S, Se, Te). *Physical Review B*, 95(23): 235434, 2017.

[40] Thanh Tien, N., Thi Bich Thao, P., Thi Han, N., Khuong Dien, V. Symmetry-driven valleytronics in the single-layer tin chalcogenides SnS and SnSe. *Physical Review B*, 109(15): 155416, 2024.

[41] Zhang, Y., Shang, B., Li, L., Lei, J. Coupling effects of strain on structural transformation and bandgap engineering in SnS monolayer. *RSC advances*, *7*(48): 30327–30333, 2017.

[42] Kaner, N.T., Wei, Y., Jiang, Y., Li, W., Xu, X., Pang, K., Li, X., Yang, J., Jiang, Y., Zhang, G., Tian, W.Q. Enhanced shift currents in monolayer 2D GeS and SnS by strain-induced band gap engineering. *ACS omega*, *5*(28): 17207–17214, 2020.

[43] Maity, N., Srivastava, P., Mishra, H., Shinde, R., Singh, A. K. Anisotropic Interlayer Exciton in GeSe/SnS van der Waals Heterostructure. *Journal of Physical Chemistry Letters*, 12(7): 1765–1771, 2021.

[44] Torun, E., Miranda, H. P. C., Molina-Sánchez, A., Wirtz, L. Interlayer and intralayer excitons in MoS_2/WS_2 and $MoSe_2/WSe_2$ heterobilayers. *Physical Review B*, 97(24): 245427, 2018.

[45] Latini, S., Winther, K. T., Olsen, T., Thygesen, K. S. Interlayer Excitons and Band Alignment in MoS_2/hBN/WSe_2 van der Waals Heterostructures. *Nano Letters*, 17(2): 938–945, 2017.

[46] Gao, S., Yang, L., Spataru, C. D. Interlayer Coupling and Gate-Tunable Excitons in Transition Metal Dichalcogenide Heterostructures. *Nano Letters*, 17(12): 7809–7813, 2017.